Ocean Engineering 228 (2021) 108871

Contents lists available at ScienceDirect

Ocean Engineering

journal homepage: www.elsevier.com/locate/oceaneng

Rapid deterministic wave prediction using a sparse array of buoys

Alexander Fisher *, Jim Thomson, Michael Schwendeman

Applied Physics Laboratory, University of Washington, Seattle, WA, USA

ARTICLE INFO

Keywords:
Irregular ocean waves
Sea surface reconstruction
Phase-resolved modeling
Data-driven prediction

ABSTRACT

A long-standing problem in maritime operations and ocean development projects has been the prediction of instantaneous wave energy. Wave measurements collected using an array of freely drifting arrays of Surface Wave Instrument Float with Tracking (SWIFT) buoys are used to test methods for phase-resolved wave prediction in a wide range of observed sea states. Using a linear inverse model in directionally-rich, broadbanded wave fields can improve instantaneous heave predictions by an average of 63% relative to statistical forecasts based on wave spectra. Numerical simulations of a Gaussian sea, seeded with synthetic buoys, were used to supplement observations and characterize the spatiotemporal extent of reconstruction accuracy. Observations and numerical results agree well with theoretical deterministic prediction zones proposed in previous studies and suggest that the phase-resolved forecast horizon is between 1–3 average wave periods for a maximum measurement interval of 10 wave periods for ocean wave fields observed during the experiment. Prediction accuracy is dependent on the geometry and duration of the measurements and is discussed in the context of the nonlinearity and bandwidth of incident wave fields.

1. Introduction

Real-time, phase-resolved reconstruction of irregular ocean waves is critical for optimizing many offshore operations ranging from developing early warning systems for surface vessels to reducing fatigue loads on offshore structures. Recent expansions in ocean development projects, including offshore wind power generation, face obstacles in achieving safe and efficient operation in an environment where unpredictable ocean waves can excite movement of a floating structure (e.g. Ma et al., 2018). For many years, spectral wave forecasts have been used in the design and operation of marine technologies, where phase-averaged statistical properties of the wave field are used to generate a stochastic prediction. The ability to deterministically predict the evolution of the sea surface wave-by-wave; however, can increase operational envelopes and help mitigate environmental loading on structures at sea. For example, wave energy converters (WECs) are typically tuned for gross average wave power (Drew et al., 2009), but the assimilation of phase-resolved wave predictions into advanced control techniques can produce significant gains in efficiency (Li et al., 2012).

Reconstruction of broadband, irregular wave fields from limited measurements is a challenging task that requires inverting a model describing wave dynamics based on limited measurements (Wu, 2004; Nouguier et al., 2014; Connell et al., 2015; Qi et al., 2018b; Desmars et al., 2020). When properly inverted, the solution can be propagated forward (backward) in time and space using the dispersion relation to produce a forecast (hindcast) at a location of interest. Morris et al. (1998) first suggested that for some measurement interval there exists a finite zone in space–time where the sea surface can be accurately reconstructed from observations. Within this theoretical prediction zone, it is feasible to accurately predict instantaneous wave elevation and related fields over short periods (Wu, 2004; Naaijen et al., 2014; Qi et al., 2018a).

The development of remote sensing technologies, such as LIDAR and X-band radar, has prompted investigations into the utility of these large spatiotemporal datasets in producing phase-resolved predictions. With adequate processing, wave information can be extracted from these raw remote sensing observations and used to perform spatio-temporal wave inversion for use in control of ship motions (Connell et al., 2015; Kusters et al., 2016; Hilmer and Thornhill, 2015; Naaijen et al., 2018; Kusters et al., 2019). Alternatively, *in-situ* measurements, such as those provided by a network of buoys, could be employed to generate wave predictions in applications where operability and/or cost prohibits the use of remote-sensing technologies. Although remote sensing observations may provide greater areal coverage, the high accuracy of point observations can provide efficient means of wave forecasting using inverse models with comparatively few degrees of freedom afforded by fewer observations.

In this paper, we present observations collected from freely drifting wave buoys and demonstrate the capability for real-time deterministic

* Corresponding author.
E-mail address: afisher@apl.washington.edu (A. Fisher).

https://doi.org/10.1016/j.oceaneng.2021.108871
Received 22 December 2020; Received in revised form 15 February 2021; Accepted 7 March 2021
Available online 10 April 2021

wave prediction in irregular, short-crested wave fields. The dataset spans a wide range of wave conditions and, to the authors' knowledge, represents the first use of *in-situ* ocean wave data in phase-resolved wave prediction using sparse multi-point measurements. Numerical simulations of a multidirectional Gaussian sea are used to assess model performance and characterize effective prediction zones. Results are discussed in the context of geometric arguments for linear prediction zones and wave group dynamics that control the modulation of instantaneous wave energy.

1.1. Wave groups

A ubiquitous feature of ocean waves is the propagation of wave energy in groups, or sets, of waves which have heights that exceed a particular threshold (Goda, 1970). High sets of waves can pose a risk to maritime operations and are fundamental to many physical processes at the ocean surface including wave breaking (Banner and Pierson, 2007; Banner et al., 2014) and rogue wave formation (Gemmrich and Thomson, 2017). Given their importance to the surface ocean and its utilization, we briefly introduce wave group formation and characteristics in regards to the spatiotemporal structure of irregular ocean waves.

Using linear wave theory, an irregular wave field can be represented as the sum of $n = 1, \ldots, N$ regular free-wave components that propagate along a horizontal plane (x,y) at some angle, θ_n, relative to the positive x-direction with an angular frequency, ω_n, and amplitude, A_n, such that the free surface can be described as:

$$\eta(x, y, t) = \mathbb{R}\left(\sum_{n=1}^{N} A_n \exp(i(\mathbf{x}\cdot\mathbf{k}_n - \omega_n t - \phi_n))\right) \tag{1}$$

where t is time, $k = \sqrt{k_x^2 + k_y^2}$, $k_x = kcos\theta$, $k_y = ksin\theta$, and frequency is related to wavenumber through the deep-water linear dispersion relation: $\omega = \sqrt{gk}$. Eq. (1) assumes that there is no mean surface current. Within this linear framework, wave groups arise from a beat frequency developing due to phase coherence between neighboring frequencies and is therefore strongly related to the scalar bandwidth of the wave energy spectrum (Longuet-Higgins, 1984):

$$\nu = \left(\frac{m_0 m_2}{m_1^2} - 1\right)^{1/2} \tag{2}$$

where m_n is the nth moment of the wave energy spectrum, $S(\omega)$. At narrow bandwidths, energy is concentrated at frequencies near the spectral peak leading to strong group structure within the wave field. As bandwidth increases, the coherency of superimposed wave components with random phases decreases leading to a reduction in the constructive and destructive interference patterns that give rise to wave groups (Thomson et al., 2019).

Wave groups can also be generated by nonlinearities within the wave field. In narrow-banded seas, four-wave nonlinear interactions can act to transfer energy from the fundamental frequency to side-band frequencies leading a periodic wave train to become unstable (Benjamin and Feir, 1967). The importance of this modulational instability (Benjamin and Feir, 1967) to the generation of wave groups can be assessed using the Benjamin–Feir Index (BFI) defined by (Janssen, 2003):

$$BFI = \sqrt{2}\left(\frac{\epsilon}{\nu}\right), \tag{3}$$

with modulational instabilities expected to occur when $BFI > 1$. Wave steepness (ϵ), defined in (4) using the peak wavenumber (k_p) and surface displacement variance ($\langle\eta^2\rangle$), is often used to assess the degree of nonlinearity within the wave field. Brackets in (4) indicate statistics calculated using short-interval measurements, typically 10–30 min of data.

$$\epsilon = \left(k_p^2 \langle\eta^2\rangle\right)^{1/2} \tag{4}$$

In addition to scalar bandwidth, directional bandwidth also acts to regulate nonlinear generation mechanisms that can give rise to high runs of waves. Previous studies of isolated wave groups in directionally-rich seas have shown that there is little to no increase in the height of the wave envelope due to nonlinear dynamics (Adcock et al., 2015, and references therein). As the directional spread of the wave field increases, wave group formation can be described effectively through interference patterns within a linear wave field (e.g. Elgar et al., 1985).

Regardless of the generation mechanism, the groupiness of irregular ocean waves necessitates that deterministic wave prediction schemes accurately capture short-duration variations in incident wave energy at the point or area of interest. Depending on the intended application, the accuracy required may range from fully phase-resolved predictions of individual waves to early warning systems based on a predicted wave envelope that exceeds a predetermined threshold.

1.2. Theoretical wave prediction zone

Given a set of measurements that span a limited space and time, phase-resolved reconstruction of an irregular wave field is constrained to a region determined by the distribution of wave energy as well as the span of the measurements. The guiding principal of this theoretical prediction zone is that the time-trace (i.e. how far did a wave travel during a sampling period) of individual observed wave packets defines a spatiotemporal zone that contains all waves incident at measurement locations during the sampling period (Morris et al., 1998; Wu, 2004; Qi et al., 2018b). Wave packets are used here to describe runs of regular wave components that propagate through the measurement domain unchanged. Recent studies have demonstrated that the prediction zone (i.e., region that extends beyond measurement locations where instantaneous wave conditions can be reconstructed) is determined by the group velocities, rather than phase velocities, of individual wave components (Wu, 2004; Blondel et al., 2010; Naaijen et al., 2014; Qi et al., 2018a). Although whole-area (X-band Radar, LIDAR, SAR, etc.) measurements of the sea surface can be used to formulate a theoretical prediction zone, we restrict our discussion to prediction zones for sparse point measurements as provided by an array of wave buoys (e.g. Raghukumar et al., 2019).

Beginning with a unidirectional irregular wave field, the prediction zone for a single point measurement is defined by the intersection of all wave packet time-traces that are observed during the sampling interval, such that the prediction zone, $\mathcal{P}$, is defined by (Wu, 2004; Qi et al., 2018b):

$$\mathcal{P}: \begin{cases} (t-T)C_{g,min} \le x - \xi \le tC_{g,max}, & T_i \le t \le 0 \\ (t-T)C_{g,min} \le x - \xi \le tC_{g,min}, & 0 \le t \le T \\ (t-T)C_{g,max} \le x - \xi \le tC_{g,min}, & T \le t \le T_f \end{cases} \tag{5}$$

where t is time, T is the measurement interval, x is the distance along wave rays, ξ is the buoy location, and C_g is a vector of group velocities for wave frequencies considered in the surface reconstruction. The temporal extent of the prediction zone, $T_i \le t \le T_f$, is then defined such that $T_i = -\beta T$ and $T_f = T + \beta T$ where $\beta = C_{g,min}/(C_{g,max} - C_{g,min})$.

When multiple point observations are used and individual buoy prediction zones overlap, the total prediction zone is bound by the maximum extent of traceable wave packets propagating through the measurement array. Geometrically, this means that the distance between buoys, δ_b, must be no larger than $C_{g,min}T$ permitting continuous tracing of all measured wave packets from one point measurement to another. The resulting total prediction zone covers a region of x–t space that is larger than the union of individual prediction zones (Figure 2 in Qi et al., 2018b). When individual prediction zones do not overlap, wave packets cannot be traced from one measurement to another and the total prediction zone becomes a discrete set of areas given by individual prediction zones (Wu, 2004; Qi et al., 2018b). Previous laboratory and simulation results have demonstrated good agreement between the theoretical prediction zone and predictions from a variety

of deterministic unidirectional wave models (Wu, 2004; Blondel et al., 2010; Naaijen et al., 2014; Simanesew et al., 2017; Qi et al., 2018a; Desmars et al., 2020).

Extending the theoretical prediction zone to multidirectional wave fields is straightforward and was recently derived in detail by Qi et al. (2018b). Predictable zones, $\mathcal{P}_N$, are obtained along specific wave propagation directions, θ_N, such that $\mathcal{P}$ is then defined as the intersection of $\mathcal{P}_N$ over all wave directions used in the sea surface reconstruction. The resulting prediction zone is a fan-shaped area that sweeps through all incident wave directions and has a maximum extent at $t = T/2$ and reduces to point locations at T_i and T_f (See Fig. 3 in Qi et al., 2018b) defined as:

$$T_i = \frac{\left(U - C_{g,min}\right) cos\theta_h T}{\left(C_{gmax} - C_{gmin} cos\theta_h\right)} \tag{6}$$

$$T_f = \frac{\left(C_{gmax} - U\right) T}{\left(C_{gmax} - C_{gmin} cos\theta_h\right)} \tag{7}$$

U is the velocity of the measurement probe and θ_h is the half-directional bandwidth of the incident wave field (Qi et al., 2018b). Eq. (7) assumes that the velocity of the probe is less than the minimum group velocity used in the reconstruction. If a measurement probe is moving at a speed of $C_{g,min} \leq U \leq C_{g,max}$, the prediction zone is nullified due to aliasing that occurs when tracing the wave component that satisfies $U = C_g$.

The rapid decay of the prediction zone following a measurement interval presents a significant challenge for real-time forecasting using sparse point measurements. Unlike whole area measurements that permit the use of 2D or 3D FFTs (Blondel-Couprie and Naaijen, 2012; Naaijen and Blondel-Couprie, 2012) in sea surface reconstruction, directly reproducing the observed 3D sea surface using Fourier decomposition is not possible using a sparse array of point measurements. In many applications, however, operational and cost constraints may favor the installation of buoy networks prompting further investigating into the possibility for their use in phase-resolved wave reconstruction. As such, alternative prediction schemes should be developed that can reconstruct (or forecast) an incident wave field for a target of interest based on limited point observations on time scales less than $T_f - T$ seconds. While several studies have investigated unidirectional irregular wave reconstruction, comparison of the theoretical prediction zone for multidirectional ocean waves remains an open question.

2. Methods

2.1. Data collection

Wave data were collected between December 6–19, 2019 in the northeastern Pacific using freely drifting arrays of Surface Wave Instrument Float with Tracking (SWIFT) buoys. Between four and six SWIFTS were deployed daily from the R/V *Sikuliaq* while in transit from Dutch Harbor, Alaska to Seattle, Washington and conducting operations at Ocean Weather Station Papa (Fig. 1a). The daily deployments collected contemporaneous wave measurements for approximately 8 h each day. Array geometries varied over the course of the experiment, but typically had buoy spacings (δ_b) on the order the observed peak wavelength (Fig. 1b-d). The buoys have a windage of approximately 1% and were drogued at a depth of 3 m to reduce drift under wind speeds that ranged from 4 m/s to in excess of 30 m/s. A summary of SWIFT observations used in this study in shown in Table 1. Data used in the analysis is restricted to typical ocean wave conditions observed during the cruise where $2 < H_S < 5$ meters and $7 < T_P < 15$ s, omitting the extreme event observed between December 11–13, 2019 where wave heights exceeded 10 meters (during which only two buoys were deployed).

In addition to four of the latest generation (v4) SWIFT buoys (Thomson et al., 2019) used throughout the experiment, two version 3 (v3) SWIFTs (Thomson, 2012) were also deployed when available. Both

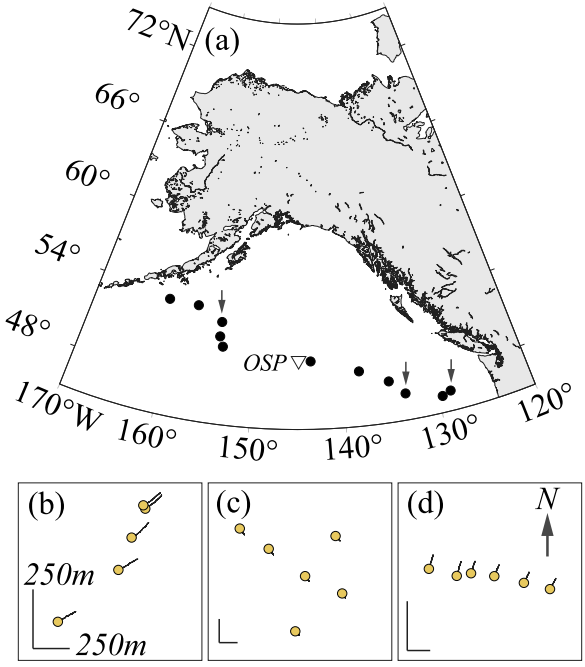

Fig. 1. (a) Map showing deployment locations in the NE Pacific. Ocean Station Papa is denoted as OSP. (b–d) Sample array geometries shown with buoy drift tracks (black lines) for December 8, 18, and 19, respectively. Spatial scale shown at lower left. Black arrows in panel (a) indicate location of sample arrays within the cruise track.

SWIFT designs measure waves using a combination of vertical accelerations and GPS velocities. Heave data are collected at 5 Hz (25 Hz) in 512 (520) second bursts every 12 min onboard the SWIFT v4 (v3). GPS velocities are collected at 5 Hz by SWIFT v4 and 4 Hz by SWIFT v3. The first portion of each burst is screened to remove poor data that results from insufficient satellite signal. Raw vertical accelerations are then rotated from a body reference frame to an earth reference frame and double-integrated to produce estimates of raw heave. A high-pass filter is applied to raw accelerations to remove low-frequency (f < 0.05 Hz) noise prior to double integration (Thomson et al., 2018). Raw measurements are used to calculate standard bulk and spectral wave parameters (Fig. 2a, Thomson, 2012; Thomson et al., 2019) as well as estimate directional spectra using a maximum entropy method. Wave envelopes, $A(t)$, are calculated as the amplitude of the analytic signal computed from the Hilbert transform of raw vertical displacement time series. A sample time series of raw vertical heave measured on December 18, 2019 is shown in Fig. 2b along with the corresponding wave envelope, smoothed using a low-pass butterworth filter with cutoff frequency equal to m_1/m_0. Finally, SWIFT v4 buoys are equipped with an ethernet bridge enabling real-time broadcasting of observed wave motions. Although this capability is not used here, it is important to note that the measurements presented are representative of data available for near real-time wave prediction.

2.2. Irregular wave reconstruction

Various strategies for deterministic wave prediction have emerged in the last two decades ranging from linear plane wave approximations (Connell et al., 2015; Desmars et al., 2020) to pseudo-spectral methods (Dommermuth and Yue, 1987; Wu, 2004; Blondel et al., 2010; Yoon et al., 2016; Qi et al., 2018a; Fujimoto and Waseda, 2020) capable of modeling the nonlinear evolution of steep wave fields. The initialization of forward-solving models, such as high-order spectral methods (HOS), can be computationally prohibitive for real-time forecasting (Desmars et al., 2020; Fujimoto and Waseda, 2020) in multidirectional ocean wave fields, suggesting that a comparatively

Table 1
Available contemporaneous measurements and average wave conditions for December 8 and 16–19, 2019.

Date	Mode (N_{SWIFT})	δ_b [m]	H_s [m]	T_p [sec]	$\overline{\sigma(f)}$ [deg]	Drift speed [m/s]
12/08/2019	5	167	3.01	8.6	39.8	0.31
12/16/2019	5	401	3.06	13.6	26.0	0.20
12/17/2019	5	503	4.38	13.7	37.2	0.18
12/18/2019	5	341	2.86	12.0	42.9	0.32
12/19/2019	6	280	3.29	12.8	33.1	0.15

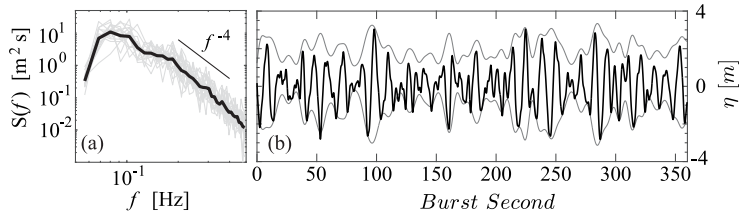

Fig. 2. (a) Sample scalar spectra collected on December 18, 2019. Black line indicates daily average. (b) Filtered heave time series measured at 22:00:00 UTC shown with a filtered wave envelope estimated using a Hilbert transform.

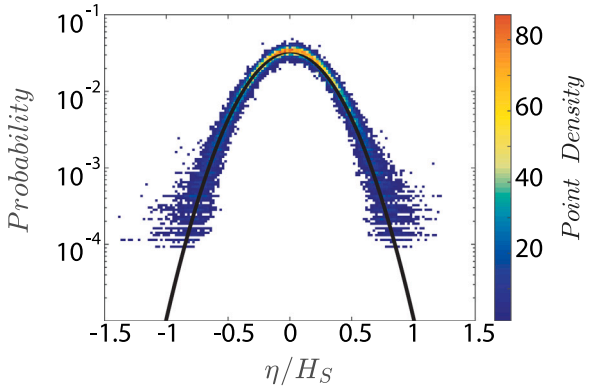

Fig. 3. (a) Measured daily histograms of normalized sea surface elevations, η/H_S, shown with fitted Gaussian distributions.

simple inverse modeling approach may offer advantages in certain applications depending on the level of accuracy required.

Following Connell et al. (2015), Eq. (1) can be expressed in matrix form and used to reconstruct the free surface from measurements of vertical displacement:

$$\eta = \mathbf{PB} \tag{8}$$

where B is a $N \times 1$ vector of unknown complex amplitudes and $\mathbf{P}$ is a $M \times N$ propagator matrix that describes the evolution of individual plane waves in space and time, such that:

$$P_{m,n} = \exp\left(i\left(\mathbf{x}_m \cdot \mathbf{k}_n - \omega_n t_m\right)\right). \tag{9}$$

If the linear system of equations shown in (8) is overdetermined ($M > N$), M measurements of vertical displacement can be used to decompose the irregular free surface into N free wave components with Fourier amplitudes, B, using a least-squares approach. Directional ambiguity in multidirectional wave fields requires that an observation has at least three degrees-of-freedom in order to resolve the directional spectrum of wave energy (e.g. Longuet-Higgins, 1961). When measurements of horizontal velocities are available, $\mathbf{P}$ can be extended to a $3M \times N$ matrix to aid in the decomposition of short-crested irregular waves in a straightforward manner, such that:

$$\begin{vmatrix} \tilde{\eta}_m \\ \tilde{u}_m \\ \tilde{v}_m \end{vmatrix} = \begin{vmatrix} \exp(i\boldsymbol{\Phi})_{m,n} \\ \frac{k_x}{k}\omega\exp(i\boldsymbol{\Phi})_{m+M,n} \\ \frac{k_y}{k}\omega\exp(i\boldsymbol{\Phi})_{m+2M,n} \end{vmatrix} B_n \tag{10}$$

where $\boldsymbol{\Phi} = \mathbf{x}_m \cdot \mathbf{k}_n - \omega_n t_m$ and $\tilde{\eta}$, $\tilde{u}$, $\tilde{v}$ indicate predicted displacement and horizontal velocities, respectively. By inverting equation (8) or (10) and solving for unknown component amplitudes and phases, a reduced-order approximation of the free surface can be projected in space and time to yield predictions of instantaneous wave conditions at a target location over a finite reconstruction horizon.

To avoid overfitting of the least squares solution to limited observations, a constrained least squares approach is used in which component amplitudes are bound by observed directional wave energy distributions (i.e., spectra) and the system is solved using an efficient trust-region reflective algorithm that provides a solution at first-order optimality based on a Newton approach for optimization (Coleman and Li, 1996). Previous studies have used Tikhonov regularization to avoid overfitting (Connell et al., 2015; Desmars et al., 2020); however, constraining the solution based on readily available directional wave spectra provided by measurements provides a more stable solution that is consistent with the observed wave field. To simplify the mathematical solution of the constrained least squares problem, the propagator matrix is transformed to represent the real part of Eq. (10) as the sum of sines and cosines via Euler's formula, increasing the number of unknowns from N to $2N$. The resulting bound-variable least-squares problem can be expressed as follows:

$$\min_x \frac{1}{2}\|\mathbf{PB} - x\|_2^2 \tag{11}$$

where x denotes the $3M \times 1$ vector of observations shown on the l.h.s of Eq. (10) and is subject to $-a \le \mathbf{B} \le a$, where a is a component-wise upper bound on the magnitude of unknown wave amplitudes. We note that sine–cosine pairs used to express each real wave component are bound by the same value of a.

Following the collection of a contemporaneous wave burst, the solution space is specified *a priori* based on the number of measurements available and the average observed directional wave spectrum estimated from the previous hour of available displacement and surface velocity data. The frequency range is limited to frequencies that satisfy $S(\omega)/max(S(\omega)) > 5\%$ (Desmars et al., 2020) and directional range is limited to $DTp - \pi/2 < \theta < DTp + \pi/2$, where $S(\omega)$ is the scalar wave energy spectrum and DT_p is the peak wave direction. The solution is limited to 40 logarithmically-spaced frequency components and 25 directional components. The upper bound for the magnitude of wave amplitudes (a) was specified by interpolating component amplitudes provided by the observed directional wave spectrum to the solution space and normalizing to preserve variance.

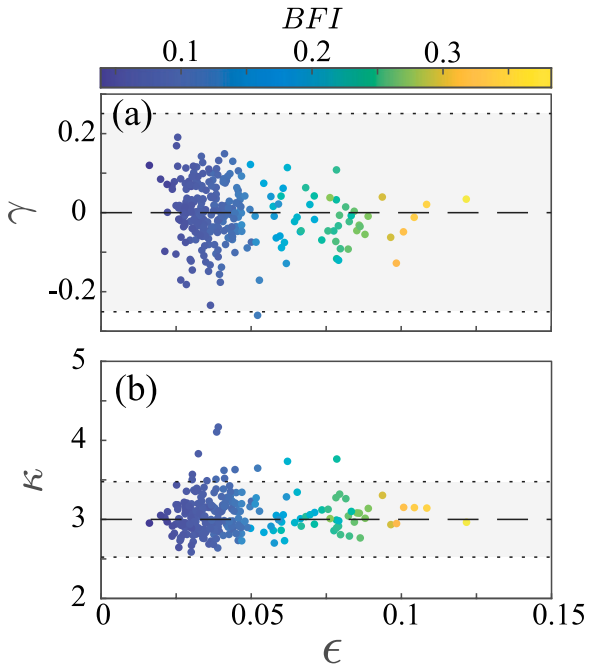

Fig. 4. (a) Wave asymmetry and (b) kurtosis versus wave steepness for all SWIFT wave bursts. Colorscale indicates the Benjamin–Feir Index calculated using Eq. (3). Dashed lines indicate Gaussian scaling. Gray areas in both panels indicates standard deviations for estimates of γ an κ based on the size of a normal sample.

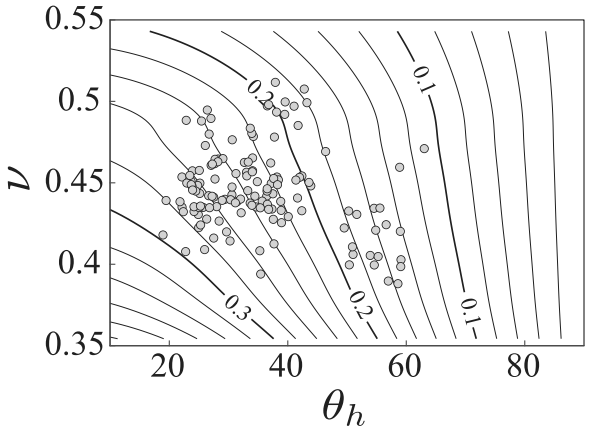

Fig. 5. Single buoy theoretical prediction horizon as a function of scalar and half-direction bandwidth. Contour lines indicate normalized forecast horizon, T_f/T (i.e. the fraction of the measurement interval that can be predicted ahead). Measured scalar bandwidth and energy-weighted average spread are shown as gray circles.

3. Results

3.1. Linearity of observed ocean waves

To assess the applicability of a linear decomposition of observed ocean waves, measured vertical displacement time series from SWIFTs are compared to probability distributions and bulk statistical metrics expected for a Gaussian sea. For each contemporaneous 8 min record, a normal distribution is fit to measured η time series from all available SWIFT buoys and goodness of fit is determined using a χ^2 test at the 5% significance level. Results are shown in Fig. 3 and are normalized by H_S.

Approximately 80.5% of measurements indicate that the surface elevation distributions are consistent with a Gaussian sea. The remaining 19.5% of data that do not follow a normal distribution were observed throughout the deployment period under a variety of wind and wave conditions. Following a similar procedure used in Thomson et al., estimates of wave steepness (4) and BFI (3) are compared to the kurtosis (12) and skewness (13) of observed wave records to further assess the role of nonlinearities in generating high runs of waves:

$$\kappa = \frac{\langle \eta^4 \rangle}{\langle \eta^2 \rangle^2} \tag{12}$$

$$\gamma = \frac{\langle \eta^3 \rangle}{\langle \eta^2 \rangle^{3/2}} \tag{13}$$

where κ is the fourth moment of the surface elevation normalized by the second moment and γ is the normalized third moment. While κ is related to BFI and includes measures of nonlinearities that arise from four-wave interactions, γ is useful in diagnosing triad interactions that are theoretically limited to wave group formation in shallow water (Peregrine, 1967; Madsen and Sørensen, 1993).

As shown in Fig. 4, ϵ ranges from 0.01 to 0.1 throughout the experiment with the majority of observations having low steepness values of $\epsilon < 0.05$. The cluster of points with $\epsilon \approx 0.1$ were collected on December 8 and December 10, 2019 when opposing seas acted to increase wave steepness. Both the increase in steepness and the directional spread of wave energy on these days suggest that (1) a linear wave model may be insufficient for capturing dominant wave dynamics and (2) there is little to no predictability at a future state based on the geometric arguments of Qi et al. (2018b). The remainder of the data generally follows the expected scaling for a Gaussian sea ($\kappa = 3, \gamma = 0$), shown as dashed lines in Fig. 4, and have BFI<1 suggesting that modulational instability did not play a significant role in wave group formation throughout much of the observational record.

The short duration of the measurements warrants further discussion about the uncertainty of statistical measures used in assessing the presence of a Gaussian wave field. Following Joanes and Gill (1998), we calculate the uncertainty of κ and γ estimates for a normal sample based on the average number of waves, estimated using a zero-crossing method, observed in the 8-minute records. As shown in Fig. 4, statistical measures calculated from relatively small sample sizes of 50–60 waves generally fall within one standard deviation of expected values for a normal distribution. This suggests that the scatter shown in Fig. 4 is primarily a result of sample size and that the majority of measurements follow a normal distribution.

Consistent with previous studies (Goda, 1983; Elgar et al., 1984; Battjes and Van Vledder, 1984; Toffoli et al., 2010; Adcock et al., 2015; Thomson et al.), these results indicate that individual wave groups observed in broadbanded, directionally-rich seas are primarily generated by the linear superposition of random wave components. However, transient nonlinearities likely play a key role in modulating the steepness and speed of dominant waves within dispersive, weakly-nonlinear wave groups; acting to increase the celerity of steepening crests to maintain propagation speeds close to that predicted by linear theory (Banner et al., 2014). Over short prediction horizons of a few wavelengths, a simple linear decomposition of the sea surface is therefore a reasonable approach to deterministic wave prediction in directionally-rich seas with low steepness.

3.2. Instantaneous wave predictions

Using the drifting arrays of SWIFTs, a data-denial experiment is used to validate the inverse modeling approach for phase-resolved wave prediction at a target location. Data from the furthest down-wave buoy (target buoy), defined using the peak wave direction, is withheld from the surface reconstruction and used to validate predictions at the location of the target buoy. Measured time series of vertical displacement and horizontal surface velocities from the remaining SWIFTs are used in the construction of the propagator matrix. Using a prescribed lead time of 5 s and a sliding measurement interval (T) of $T/T_{m0} = 9$,

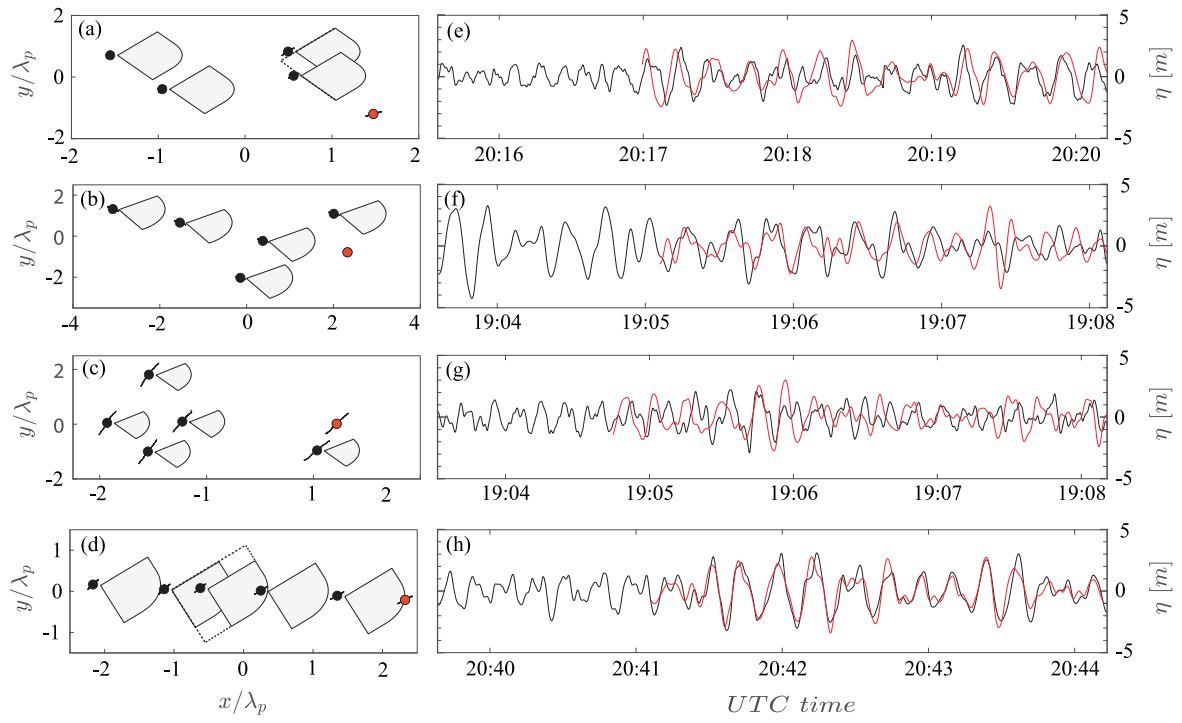

Fig. 6. (a–d) Sample drifting buoy array geometries for Dec 16–19, respectively, shown with theoretical prediction zones (gray areas). The total $\mathcal{P}$ for multiple overlapping zones are shown as unshaded areas. Red markers indicate the target buoy and solid lines show the drift track of the buoys during the measurement interval. (e–h) Corresponding measured surface elevation time series, η (black), shown with least-squares predictions, $\tilde{\eta}$ (red), at the target buoy location.

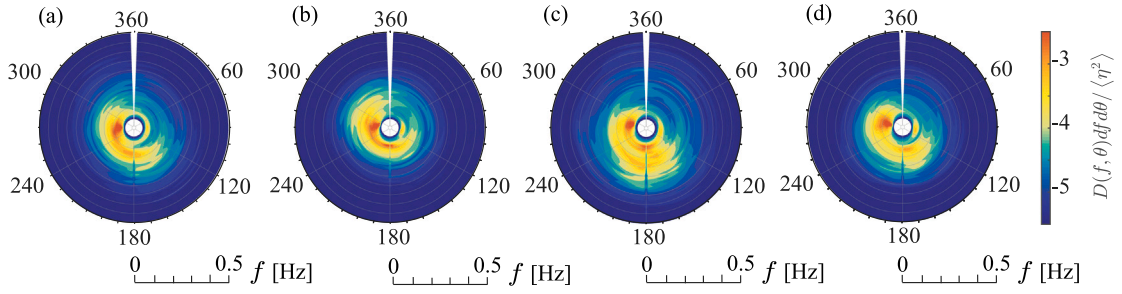

Fig. 7. Measured 1-h average directional wave spectra, normalized by the surface displacement variance, for December 16–19, 2019 (a–d), respectively.

where T_{m0} is the average observed wave period, vertical displacement was forecasted at the target buoy location 5–6 s into the future. The resulting propagator matrix constructed from raw 5 Hz time series had approximately $O(10^8)$ elements and could be used to solve for $O(10^3)$ unknown complex free wave amplitudes in ≈1 s on a generic laptop with a quad-core 2.8 GHz processor.

To illustrate theoretical environmental prediction constraints for wave conditions observed in this experiment, Fig. 5 shows the estimated normalized prediction horizon of a single point measurement, T_f/T, as a function of scalar and directional bandwidth. Contour lines of normalized prediction horizons (7) are calculated by determining the frequency range needed to model a two-parameter Bretschneider spectrum based on the criterion specified in Section 2. A range of scalar bandwidths were generated by varying the peakedness factor from 4 to 15 and the slope of the spectral tail at frequencies greater than peak frequency from −5 to −4. Observations are plotted using estimated scalar bandwidths and energy-weighted average directional spread, $\overline{\sigma(f)}$.

For observed wave conditions, a conservative estimate of the temporal forecast horizon from a network of point measurements is limited to between 10% and 30% of the measurement duration. As scalar bandwidth and directional spread increase, that horizon decreases until it eventually reaches zero when incident waves are coming from opposite directions. For the remainder of this paper, results will be limited to data from December 16–19, 2019 when at least 4 forecasting buoys were available and the directional distribution of wave energy permitted short-range forecast horizons of $O(10)$ seconds based on $O(100)$ seconds of measurements.

Fig. 6e–h shows wave predictions at the target buoy locations shown in panels (a–d) for sample bursts collected between December 16–19, 2019. Shaded areas in Fig. 6a-d indicate individual buoy linear prediction zones calculated following Qi et al. (2018b), with dashed lines indicating the effective array prediction zone for overlapping buoy prediction zones. In many cases, the down-wave target buoy was located outside of the predictable zone for the measurement array, such that a surface reconstruction from observations at forecasting buoys is expected to deviate from instantaneous conditions at the target buoy. This is generally consistent with the results; however, predicted $\tilde{\eta}$ time series reasonably capture the amplitude and phase of the larger individual waves in many cases.

Sample predictions shown for December 16–18 highlight two different challenges for deterministic wave prediction from sparse measurements. On December 16, the target buoy was located southeast of the measurement array when waves were predominantly out of the west. The relative azimuth of the target buoy fell in a sidelobe of

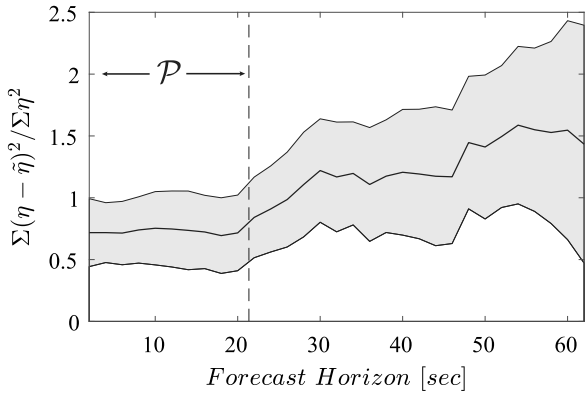

Fig. 8. Prediction error between Dec. 19 target buoy measurements and predictions for lead times between 0–60 s. Black line indicates median error and the gray area represents ±1 standard deviation. Dashed vertical line indicates maximum extent of $\mathcal{P}$.

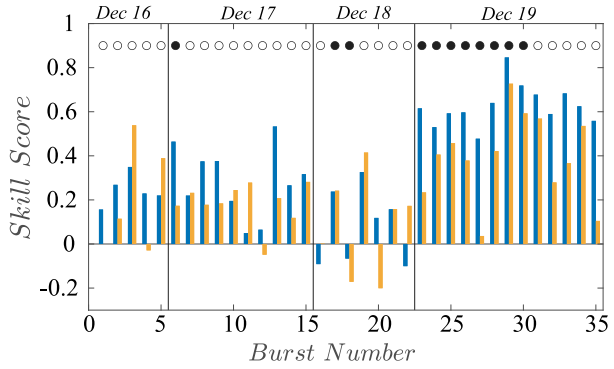

Fig. 9. Mean square error skill score relative to spectral null forecast for instantaneous heave (blue) and wave envelope (yellow) for December 16–19, 2019. Open and filled markers indicate arrays of 5 buoys and 6 buoys, respectively.

wave energy passing through the array, where short-crestedness likely limited the correlation between wave envelopes measured by the array and those incident at the target buoy during the measurement period. In contrast, the erroneous predictions on December 17–18 were the combined result of array geometry and large directional bandwidth. Southerly swell propagated through the measurement domain between Dec 17–18 (Fig. 7), resulting in a complex wave field composed of two nearly perpendicular wave systems. This likely reduced the predictability of instantaneous wave energy as individual wave components were reaching the target location(s) and the measurement array at similar times.

On December 19, waves were principally out of the west and the target buoy was located within the predictable zone of the closest upwave buoy (Fig. 6g) throughout the deployment. With a buoy spacing of $\delta_b \approx \lambda_p$, where λ_p is the peak wavelength, only two of the individual buoy prediction zones overlapped for a measurement interval of $9T_{m0}$ (Fig. 6d). Despite discontinuous time-traces of wave packets being used to fit wave components in the surface reconstruction, the strong agreement between predicted and observed surface elevation shown in Fig. 6h suggests that predictive skill of the array is generally consistent with the theoretical prediction zone proposed in previous studies.

To compare prediction accuracy over the extent of the theoretical prediction zone, the prescribed lead time used in generating predictions at the target buoy was varied between 0 and 60 s. Results for December 19 are shown in Fig. 8 along with the extent of the linear prediction zone for the measurement array. Prediction error is quantified using a normalized mean square error between predicted and observed vertical displacements. Up to 20 s after the completion of a sampling burst, the surface reconstruction demonstrates some skill in predicting surface elevation at the target buoy, which is consistent with the maximum range of the linear prediction zone. Beyond that time, errors increase as unmeasured waves reach the target location and nullify the forecasted wave field structure. The results shown in Figs. 6 and 8 indicate that the simple linear inverse model used here is capable of generating deterministic predictions of an irregular wave field over a temporal forecast horizon of $O(10)$ seconds. Furthermore, phase-resolved predictions could be used to produce remote measurements of waves in a reconstruction mode ($T/2$) at locations that would normally prevent *in-situ* data collection. For example, a data-driven estimate of instantaneous wave loading on a floating structure where reflection and dampening would otherwise prevent direct wave measurements.

To quantify the skill of the inverse model relative to state-of-the-art spectral models currently used in marine forecasting, a mean-square-error skill score is defined as:

$$Skill\ Score = 1 - \frac{MSE_p}{MSE_s} \tag{14}$$

where MSE_p and MSE_s are the mean square errors between $\tilde{\eta}(t)$ and $\eta(t)$ at the target buoy, for the inverse linear model and spectral wave model, respectively. Surface elevation time series used in MSE_s are generated from the summation of wave components with amplitudes drawn from a Rayleigh distribution described by the observed wave spectrum with randomized phase. In an ensemble sense, MSE_s was generally less (larger) than observed mean values of η^2 when evaluated for wave envelope (surface displacement) time series. Some skill is achieved when comparing amplitude errors for irregular wave time series with similar groupiness, but the combination of phase and amplitude errors increases the MSE_s of surface elevation beyond average measured η^2.

Fig. 9 shows the median skill scores for both surface displacement and wave envelope, estimated from 50 synthetic realizations, as well as the number of buoys available for prediction. The influence of array geometry and spectral bandwidth is clear with a notable increase in skill on December 19 when buoys were deployed in a linear array aligned with dominant wave direction and wave energy was principally out of the west (Fig. 7d). The lowest skill scores occurred on December 18 when mixed seas limited the predictability of instantaneous wave heights. In most cases, the simple inverse linear model increased accuracy up to 80% (70%) for deterministic wave elevation (envelope) prediction relative to modern spectral forecasts demonstrating the potential for real-time forecasting of instantaneous wave conditions despite the limitations of drifting buoy geometries.

4. Discussion

The differences in approach between a forward-solving dynamical simulation and an inverse least-squares model warrant further discussion regarding the spatiotemporal prediction horizon and measurement constraints for the approach used here. While a forward-solving assimilative model relies on accurate initialization to simulate the evolution of the velocity potential (Wu, 2004; Qi et al., 2018a; Desmars et al., 2020; Fujimoto and Waseda, 2020), the inverse model approximates the shape and evolution of observed wave envelopes using a simple summation of plane waves fit to the observed free surface. Both approaches are dependent on the resolution of the solution space and as such are reduced-order representations of real short-crested seas that manifest from a continuum of scalar and directional wave components. In the following sections, the effective prediction zone is characterized in the context of short-crested wave geometry and limitations on the duration of measurement record and the number of buoys used in inverse modeling the free surface are discussed.

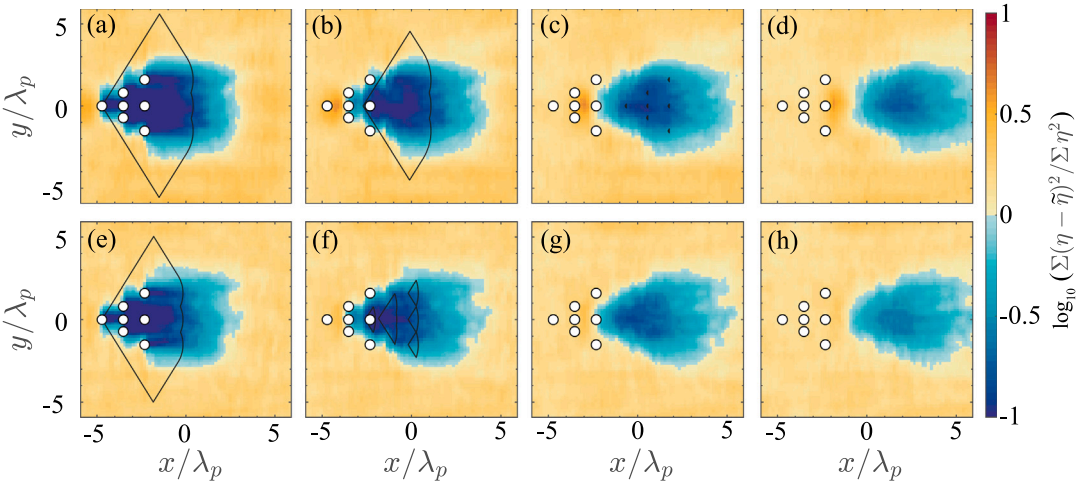

Fig. 10. Mean reconstruction error based on 7 point measurements sampling a synthetic Gaussian wave field. Panels (a–d) represent waves simulated from a JONSWAP spectrum at $T_f = 0, 10, 20, 30$ seconds, respectively. Panels (e–h) are the same as (a–d) except simulated using a Bretschneider spectrum with f^{-4} tail, respectively. In all panels, solid lines indicate the linear prediction envelope.

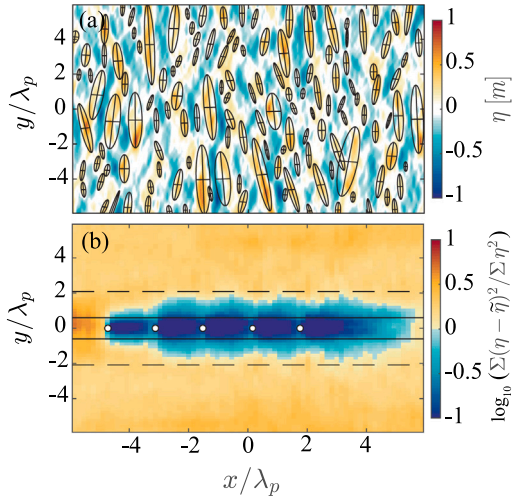

Fig. 11. (a) Sample crest detection for the synthetic wave field used in Fig. 8. Black ellipses are fit to wave crests with mean curvatures >0.01 m^{-1}. (b) Comparison of average prediction error from linear buoy array with crest length statistics. Solid black line indicates the average crest length and the dashed line indicates the 95th percentile.

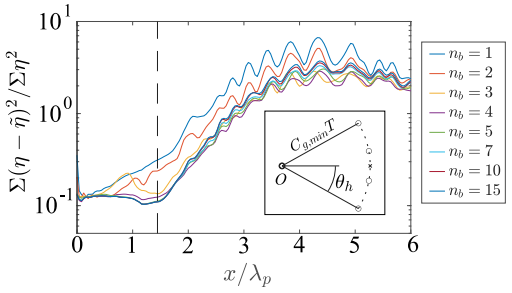

Fig. 12. Sensitivity of prediction error to the number of buoys used in forecasting. Dashed vertical line indicates maximum extent of $\mathcal{P}$ down-wave of measurement array. Inset shows array geometry with locations of $n_b = 5$ artificial buoys.

4.1. Effective prediction zone

The effective prediction zone is characterized using synthetic wave fields generated using the Wave Analysis for Fatigue and Oceanography (WAFO) MATLAB toolkit (WAFO-group, 2000). This enables exploration of spatial dependence beyond the buoy array geometries tested during the field experiments. Spectral simulations of a Gaussian sea are performed using 2D FFTs on a uniform 300 m x 300 m grid with resolutions between 2-5 m and a time step of 0.2 s. Directional wave spectrum used in the simulations are specified using a 256-point frequency vector and 2 degree directional bins. The simulation period was 400 s.

To compare the effective prediction zone to the theoretical prediction zone, WAFO is used to simulate a similar scenario as that shown in Figure 14 of Qi et al. (2018b). Time series from seven locations within the wave field representing an artificial buoy array (Fig. 10a) are used to generate least-squares forecasts of the sea surface and compared to the spatiotemporal extent of the theoretical prediction zone. Two directional design spectra were specified with 4 s peak wave periods, T_p, and 1 meter significant wave heights: (1) a standard JONSWAP spectrum ($\nu = 0.36$, panels a–d) and (2) a Bretschneider spectrum ($\nu = 0.45$, panels e–h) with a peakedness factor of 4 and a f^{-4} tail representing a fully-developed wind sea. A uniform spreading function is applied to all wave frequencies that follows $D(\theta) = cos(\pi\theta/(2\Theta_0))^2/\Theta_0$, where $\Theta_0 = \pi/6$. For consistency, a measurement duration of $T = 10T_p$ is used in the generating predictions. Prediction error is then assessed across the full simulation domain at $t = T, T + 10, T + 20$, and $T + 30$ seconds into the future.

As scalar bandwidth increases, the frequency range required to model the wave field also increases and the prediction horizon decreases per (7). Differences between panels (a–d) and (e–h) of Fig. 10 illustrate the effects of increasing bandwidth on the spatiotemporal range of predictability. The maximum forecast horizon for the JONSWAP and Bretschneider simulations are $0.52T$ and $0.27T$, respectively. Due to increased wave energy in the high frequency range of the spectrum, the spatial extent of the theoretical Bretschneider prediction zone is smaller than the JONSWAP prediction zone. The combined effect of reduced forecast horizon and smaller horizontal extent leads to the separation of individual buoy prediction zones earlier in the Bretschneider simulation, such that the decorrelation of measured wave time series leads to reduced prediction windows relative to the JONSWAP simulation. These results demonstrate the importance of bandwidth in the design and implementation of deterministic wave prediction schemes when offshore wave conditions may not exhibit a spectral shape consistent with fetch-limited wave growth.

In both simulations, the least-squares approach accurately reconstructs the wave field over a subspace of $\mathcal{P}$, extending a distance of $C_{g,min}t$ down-wave, but fails to predict the sea surface at the outer

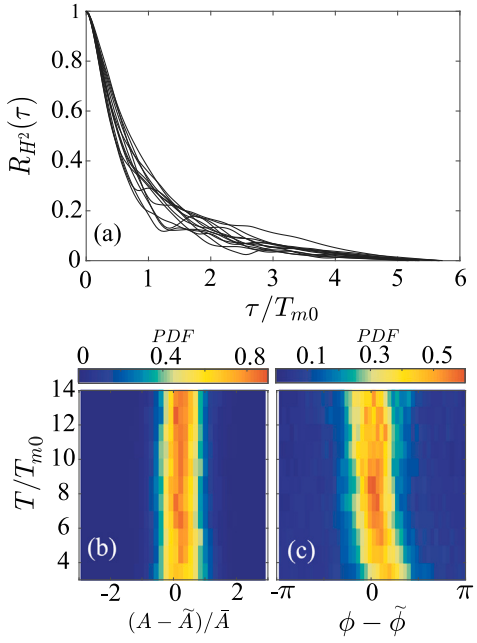

Fig. 13. (a) Envelope autocorrelation functions for December 19 observations as a function of normalized lag τ/T_{m0}. Effect of measurement duration T/T_{m0} on (b) instantaneous error between observed and predicted wave envelope and (c) instantaneous phase error between observed and predicted vertical displacement at target buoy.

lobes of the prediction zone. This can be explained by considering the surface-fitting nature of a least-squares approach to wave field reconstruction. Unlike forward-solving models that solve surface boundary conditions to determine the velocity potential, the inverse model generates an approximation of the shape of measured individual wave forms incident at buoy locations. Residuals of the fit result in a reduction in prediction accuracy at the outer lobes of the theoretical prediction zone, but the least-squares approximations exhibit some predictive skill down-wave of the theoretical prediction zone, which appears independent of bandwidth and is also evident in the observations shown in Fig. 6. High-fidelity reconstruction of the sea surface, however, is limited to a subspace of the theoretical prediction zone that extends $C_{g,min}t$ down-wave (panels a and e) indicating that scalar bandwidth acts as a control on the temporal (or along-wave) prediction horizon. This subtle difference suggests that the effective prediction zone for a least-squares solution is dependent on wave geometry and spectral bandwidth in short-crested seas and that least-squares predictions may exhibit marginal skill at $t > T_f$.

A crest length distribution of the short-crested synthetic JONSWAP wave field was estimated by fitting ellipses to wave crests and estimating the length of each crest, L_c, as the major axis of the ellipse, similar to the method used in Monaldo (2000). A curvature threshold based on the mean Gaussian curvature of the free surface was used to identify wave crests, such that crests were defined as regions that had a mean curvature less than or equal -0.01/m and an area greater than 10 square meters. A snapshot of the crest length detection routine is shown in Fig. 11a. Fig. 11b shows prediction error for the same wave field as that shown in Fig. 10a except with the 5 artificial buoys arranged in a line along the principal wave direction with $\delta_b = C_{g,min}T$. The transverse extent of the effective prediction zone reflects the distribution of incident crest lengths with the most accurate predictions occurring within 1 average crest length, $\overline{L_c}$, of the measurement line. The dependency shown in Fig. 11b is consistent with two other test cases based on uniform cos^{2s} spreading functions (not shown), but further research is needed to quantify the influence of frequency-dependent spreading functions on effective prediction zones.

This suggests that the measurement points should be positioned a distance of $\overline{L_c}$ apart in the transverse direction to maximize the effective predictable area down-wave of a measurement array. Additionally, this result differs from the cubic dependency between the number of optimally-positioned probes and prediction envelope found by Qi et al. (2018b) and suggests a linear dependency between the effective prediction envelope provided by a linear inverse model and the number of point observations.

4.2. Dependence of forecast accuracy on the number of measurements

To determine the minimum number of point measurements needed for accurate surface reconstruction, WAFO simulations, similar to those shown in Fig. 10e, are seeded with varying numbers of artificial buoys, n_b, and used to generate a prediction at $t = T$. The artificial buoys are arranged in a fan-shape with central angle of $2\theta_h = pi/3$, with one buoy located at the center of a circle (point O) with a radius of $C_{g,min}T$ (Fig. 12). Between 1 and 14 additional buoys are equally-spaced along the arc of the fan. In the case of $n_b = 1$, one point measurement was placed a distance R down-wave of O. In all cases, the maximum extent of the linear prediction zone was the same and terminated at a distance $2C_{g,min}T$ from point O.

Fig. 12 shows that prediction accuracy over the temporal extent of the prediction zone converges when $n_b \geq 4$. This result suggests that with as few as 4 buoys, accurate phase-resolved wave forecasts could be generated for a point of interest down-wave of the measurement array. The level of accuracy likely depends on the resolution of the solution space relative to the spectral energy content of the wave field. Sensitivity testing of the wave components used in the prediction is beyond the scope of this paper, but we note that adaptive optimization of the least-squares solution space may increase the accuracy of the solution in complex wave fields reconstructed from limited point measurements.

In addition to the number of measurement points used in the reconstruction, it is reasonable to assume that the accuracy of least-squares predictions are also dependent on the record length used in Eq. (8). Specifically, the decorrelation scale of irregular waves likely limits the applicability of a sea surface decomposition based on periodic, stationary wave components in an ergodic, stochastic wave field. To assess the influence of measurement duration on prediction accuracy, we estimate the decorrelation scale of measured ocean wave fields following the wave envelope approach outlined in Medina and Hudspeth (1990). The envelope autocorrelation function, $R_{H^2}(\tau)$, is related to the spectrum, $\Gamma(f)$, of the squared wave height function, $H(t) = 2A(t)$, such that the two quantities form a Fourier pair via the Wiener–Khinchin theorem as shown in (15).

$$\Gamma(f) = \mathcal{F}\left(R_{H^2}(\tau)\right) \tag{15}$$

We note that $R_{H^2}(\tau)$ is equivalent to the squared envelope of the autocorrelation function for surface displacement and can be used to describe basic characteristics of ocean wave groups in a stochastic process (Medina and Hudspeth, 1990).

Individual SWIFT heave time series are used to calculate average $\Gamma(f)$ for each contemporaneous burst and used to determine the decorrelation scale of observed wave envelopes. Envelope autocorrelation functions for wave measurements collected on December 19 are shown in Fig. 13a. Results indicate that within a time span of $4T_{m0} < \tau < 5T_{m0}$, instantaneous wave energy becomes decorrelated with itself suggesting an upper bound for the measurement interval used to fit a linear wave components to observed wave envelopes. Because the two-sided autocorrelation function is symmetric, this result indicates that the measurement interval used in the inverse model should be no longer than 10 average wave periods for the wave field observed on December 19.

To test this finding, predictions were generated using measurement intervals ranging from $3T_{m0}$ to $14T_{m0}$ for wave bursts collected on December 19 and compared to observations. Fig. 13 shows distributions

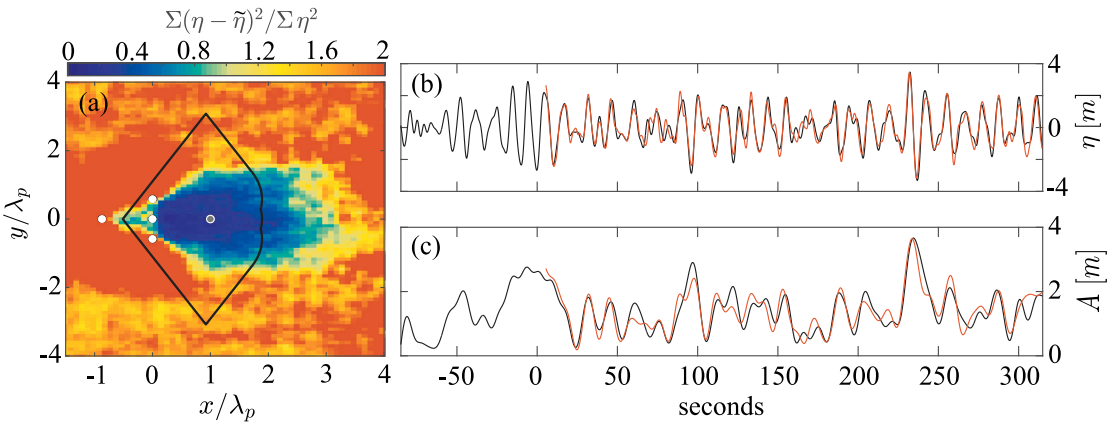

Fig. 14. (a) Mean reconstruction error for synthetic rendering of Dec 19 data with buoy array configured to predict wave energy at a fixed target location λ_p downwave (gray dot). Black line indicates theoretical linear prediction envelope. (b) Comparison of $\eta(t)$ (black) and $\tilde{\eta}(t)$ (red) at target location. (c) Comparison of simulated $A(t)$ (black) and predicted $\tilde{A}(t)$ (red) smoothed using a low-pass butterworth filter with a $m1/m0$ cutoff frequency.

of prediction errors for the normalized envelope error (b), where $\overline{A(t)}$ is the mean value of $A(t)$ observed during the prediction window, and the instantaneous phase error (c) estimated from the Hilbert transform of vertical displacement time series. In all cases, the system is overdetermined with data from at least 4 buoys available for forecasting. It is apparent that when short measurement intervals ($T < 6T_{m0}$) are used, observations contain insufficient information to accurately reconstruct the incident wave envelopes and prediction quality decreases for both amplitude and phase. Distributions of amplitude error are relatively consistent for $T \geq 6T_{m0}$, with a slight underprediction bias. In contrast, a peak in the kurtosis of the phase error distributions occurs at $T/T_{m0} = 9$. Above and below this value of T/T_{m0}, the distribution of phase errors flattens indicating a higher likelihood of erroneous predictions. This is consistent with the autocorrelation functions shown in panel (a) and suggests that constraining the measurement interval based on the decorrelation scale of expected wave envelopes improves prediction accuracy.

4.3. Example installation design

Synthesizing our results, the potential for real-time forecasting at a target location is illustrated using observations from 21:30 UTC on December 19 when four buoys arranged similarly to Fig. 6d were available for forecasting. Using the measured directional wave spectrum, WAFO was used to simulate a synthetic 3D wave field. Four artificial buoys were placed within the domain and used to forecast wave conditions at a target point located λ_p down-wave of the array (Fig. 14a). The geometry of the measurement array was modified to reflect results shown in Figs. 8 and 11. The measurement interval was set at $9T_{m0}$ and used to generate rolling 1 s predictions and specifying a lead time of 5 s.

Predicted time series of both the wave envelope and surface elevation agree well with simulated waves at the target location throughout an 8-minute simulation period and accurately capture a high-run of waves that occurred at the target location (Fig. 14b). Forecasts were generated in ≈1 s, highlighting the potential for feed-forward heave predictions for use in adaptive control and/or early-warning systems. The minimal computational effort required to produce these forecasts enables real-time forecasting while permitting a system latency of $O(1)$ seconds.

5. Conclusions

Wave observations collected by freely drifting arrays of SWIFTs were used to develop methods for near real-time, phase-resolved wave reconstruction. Under a wide range of ocean wave conditions, data-denial experiments were carried out to evaluate the effective zone of predictability and accuracy of sea surface reconstructions estimated using a least-squares inverse wave model. Results demonstrate the potential for near real-time irregular wave reconstruction from sparse point measurements and can be summarized as follows:

- In directionally-rich seas with low steepness, a linear decomposition of the wave field using a constrained least squares approach can be used to reconstruct the local wave field from as few as 4 point measurements. The sea surface reconstruction can then be propagated in space–time to yield near real-time wave predictions at a location and time of interest. This simple, novel approach improves prediction accuracy of vertical surface displacement (wave envelope) time series relative to spectral forecasts by an average of 63% (40%) during periods when the target location was within the effective predictable zone.
- Comparisons between observed and simulated wave fields and least-squares predictions is generally consistent with previous descriptions of the theoretical prediction zone for deterministic wave reconstruction. However, the transverse extent of the effective prediction zone for an inverse model is limited by wave geometry in short-crested seas, such that the surface reconstruction is accurate within one average crest length ($\overline{L_c}$) of the measurement point. This suggests a linear relationship between predictable area and the number of measurement points and that the areal extent of sea surface reconstructions can be maximized by using a transverse spacing of $\overline{L_c}$ in measurement arrays.
- When wave group structure is considered, the accuracy of the inverse model improves as it effectively acts to reconstruct coherent structures within a stochastic, irregular ocean wave field. The decorrelation scale of wave groups determines the upper bound for the duration of measurements used in an inverse model of the sea surface with observed decorrelation scales of $10T_{m0}$.
- Spectral bandwidth significantly influences the extent of the effective prediction zone such that the region of space–time over which the sea surface can be reconstructed decreases with increasing scalar and directional bandwidth. For observed wave fields, the maximum forecast horizon was estimated to be between 1–3 T_{m0} for a measurement duration of $10T_{m0}$.

Developing methods for accurate sea surface reconstruction from sparse measurements can enable theoretical investigations of wave processes in areas limited by a lack of direct observations. For example, a similar approach could be used to reconstruct instantaneous loading for process studies of wave-structure interactions, such as those that seek to improve the performance of floating turbines or WEC devices. The computational efficiency of an inverse model may also provide short-duration forecasts in near real-time for many applications ranging from

predicting sea surface conditions in denied areas to the development of adaptive control systems for ships and structures at sea.

CRediT authorship contribution statement

Alexander Fisher: Methodology, Investigation, Writing - original draft , Data curation. **Jim Thomson:** Conceptualization, Methodology, Investigation, Writing - reviewing and editing, Data curation. **Michael Schwendeman:** Methodology, Writing - reviewing and editing.

Declaration of competing interest

The authors declare that they have no known competing financial interests or personal relationships that could have appeared to influence the work reported in this paper.

Acknowledgments

Funding for this work was provided by NSF-OCE 1756040. Fisher was supported by a Science and Engineering Enrichment and Development (SEED) Postdoctoral Fellowship from the University of Washington, USA Applied Physics Laboratory (APL-UW). SWIFT buoys are built and maintained at APL-UW by Joe Talbert and Alex de Klerk, who were instrumental to all aspects of data collection. We are indebted to the captain and crew of the R/V *Sikuliaq* for their assistance throughout the experiment. Data and codes used in this study will be publicly available through the University of Washington ResearchWorks data repository: https://digital.lib.washington.edu/researchworks/handle/1773/15609.

References

Adcock, T.A.A., Taylor, P.H., Draper, S., 2015. Nonlinear dynamics of wave-groups in random seas: unexpected walls of water in the open ocean. Proc. R. Soc. Lond. Ser. A Math. Phys. Eng. Sci. 471 (20150660).

Banner, M.L., Barthelemy, X., Fedele, F., Allis, M., Benetazzo, A., Dias, F., Peirson, W.L., 2014. Linking reduced breaking crest speeds to unsteady nonlinear water wave group behavior. Phys. Rev. Lett. 112, 114502. http://dx.doi.org/10.1103/PhysRevLett.112.114502.

Banner, M., Pierson, W.L., 2007. Wave breaking onset and strength for two-dimensional deep water wave groups. J. Fluid Mech. 585, 93–115.

Battjes, J., Van Vledder, G.P., 1984. Verification of Kimura's theory for wave group statistics. In: Coastal Engineering 1984. pp. 642–648.

Benjamin, T., Feir, J., 1967. The disintegration of wave trains on deep water Part 1. J. Fluid Mech. 27 (03), 417–430.

Blondel, E., Bonnefoy, F., Ferrant, P., 2010. Deterministic non-linear wave prediction using probe data. Ocean Eng. 37 (10), 913–926. http://dx.doi.org/10.1016/j.oceaneng.2010.03.002.

Blondel-Couprie, E., Naaijen, P., 2012. Reconstruction and prediction of short-crested seas based on the application of a 3D-FFT on synthetic waves: Part 2—Prediction. In: International Conference on Offshore Mechanics and Arctic Engineering, vol. 44922. American Society of Mechanical Engineers, pp. 55–70.

Coleman, T.F., Li, Y., 1996. A reflective Newton method for minimizing a quadratic function subject to bounds on some of the variables. SIAM J. Optim. 6 (4), 1040–1058.

Connell, B.S., Rudzinsky, J.P., Brundick, C.S., Milewski, W.M., Kusters, J.G., Farquharson, G., 2015. Development of an environmental and ship motion forecasting system. In: International Conference on Offshore Mechanics and Arctic Engineering, vol. 56598. American Society of Mechanical Engineers, p. V011T12A058.

Desmars, N., Bonnefoy, F., Grilli, S., Ducrozet, G., Perignon, Y., Guérin, C.-A., Ferrant, P., 2020. Experimental and numerical assessment of deterministic nonlinear ocean waves prediction algorithms using non-uniformly sampled wave gauges. Ocean Eng. 212, 107659. http://dx.doi.org/10.1016/j.oceaneng.2020.107659.

Dommermuth, D.G., Yue, D.K., 1987. A high-order spectral method for the study of nonlinear gravity waves. J. Fluid Mech. 184, 267–288.

Drew, B., Plummer, A., Sahinkaya, M., 2009. A review of wave energy converter technology. Proc. Inst. Mech. Eng. A 223 (8), 887–902.

Elgar, S., Guza, R.T., Seymour, R.J., 1984. Groups of waves in shallow water. J. Geophys. Res. 89 (C3), 3623–3634.

Elgar, S., Guza, R.T., Seymour, R.J., 1985. Wave group statistics from numerical simulations of a random sea. Appl. Ocean Res. 7 (2), 93–96.

Fujimoto, W., Waseda, T., 2020. Ensemble-based variational method for nonlinear inversion of surface gravity waves. J. Atmos. Ocean. Technol. 37 (1), 17–31. http://dx.doi.org/10.1175/JTECH-D-19-0072.1.

Gemmrich, J., Thomson, J., 2017. Observations of the shape and group dynamics of rogue waves. Geophys. Res. Lett. 44 (4), 1823–1830, 2016GL072398, http://dx.doi.org/10.1002/2016GL072398.

Goda, Y., 1970. Numerical experiments on wave statistics with spectral simulation. Report Port Harbour Res. Inst. 9, 3–57.

Goda, Y., 1983. Analysis of wave grouping and spectra of long-travelled swell. Rep. Port Harb. Res. Inst. 22 (1), 3–41.

Hilmer, T., Thornhill, E., 2015. Observations of predictive skill for real-time deterministic sea waves from the wamos II. In: OCEANS 2015 - MTS/IEEE Washington. pp. 1–7. http://dx.doi.org/10.23919/OCEANS.2015.7404496.

Janssen, P., 2003. Nonlinear four-wave interactions and freak waves. J. Phys. Oceanogr. 33 (4), 863–884. http://dx.doi.org/10.1175/1520-0485(2003)33<863:NFIAFW>2.0.CO;2.

Joanes, D., Gill, C., 1998. Comparing measures of sample skewness and kurtosis. J. R. Stat. Soc. Ser. D Statistician 47 (1), 183–189.

Kusters, J., Cockrell, K., Connell, B., Rudzinsky, J., Vinciullo, V., 2016. Futurewaves™: A real-time ship motion forecasting system employing advanced wave-sensing radar. In: OCEANS 2016 MTS/IEEE Monterey. IEEE, pp. 1–9.

Kusters, J., Connell, B., Milewski, W., Vinciullo, V., van Dijk, R., 2019. Wave characterization and timing using doppler radar–update on the futurewaves™ wave and vessel motion forecasting system. In: OCEANS 2019 MTS/IEEE SEATTLE. IEEE, pp. 1–9.

Li, G., Weiss, G., Mueller, M., Townley, S., Belmont, M.R., 2012. Wave energy converter control by wave prediction and dynamic programming. Renew. Energy 48, 392–403. http://dx.doi.org/10.1016/j.renene.2012.05.003.

Longuet-Higgins, M.S., 1961. Observations of the directional spectrum of sea waves using the motions of a floating buoy. Ocean Wave Spectra.

Longuet-Higgins, M.S., 1984. Statistical properties of wave groups in a random sea state. Philos. Trans. R. Soc. Lond. Ser. A Math. Phys. Eng. Sci. 312 (1521), 219–250. http://dx.doi.org/10.1098/rsta.1984.0061.

Ma, Y., Sclavounos, P.D., Cross-Whiter, J., Arora, D., 2018. Wave forecast and its application to the optimal control of offshore floating wind turbine for load mitigation. Renew. Energy 128, 163–176. http://dx.doi.org/10.1016/j.renene.2018.05.059.

Madsen, P., Sørensen, O., 1993. Bound waves and triad interactions in shallow water. Ocean Eng. 20 (4), 359–388. http://dx.doi.org/10.1016/0029-8018(93)90002-Y.

Medina, J., Hudspeth, R., 1990. A review of the analyses of ocean wave groups. Coast. Eng. 14 (6), 515–542. http://dx.doi.org/10.1016/0378-3839(90)90033-S.

Monaldo, F., 2000. Measurement of wave crest length and groupiness from spaceborne synthetic aperture radar. Mar. Struct. 13(4-5), 349–366.

Morris, E., Zienkiewicz, H., Belmont, M., 1998. Short term forecasting of the sea surface shape. Inte. Shipbuild. Prog. 45 (444), 383–400.

Naaijen, P., Blondel-Couprie, E., 2012. Reconstruction and prediction of short-crested seas based on the application of a 3D-FFT on synthetic waves: Part 1-reconstruction. In: International Conference on Offshore Mechanics and Arctic Engineering, vol. 44922. American Society of Mechanical Engineers, pp. 43–53.

Naaijen, P., van Oosten, K., Roozen, K., van 't Veer, R., 2018. Validation of a deterministic wave and ship motion prediction system. International Conference on Offshore Mechanics and Arctic Engineering, Ocean Eng. International Conference on Offshore Mechanics and Arctic Engineering, 7B.V07BT06A032, http://dx.doi.org/10.1115/OMAE2018-78037,

Naaijen, P., Trulsen, K., Blondel-Couprie, E., 2014. Limits to the extent of the spatio-temporal domain for deterministic wave prediction. Int. Shipbuild. Prog. 61, 203–223. http://dx.doi.org/10.3233/ISP-140113.

Nouguier, F., Grilli, S.T., Guérin, C., 2014. Nonlinear ocean wave reconstruction algorithms based on simulated spatiotemporal data acquired by a flash LIDAR camera. IEEE Trans. Geosci. Remote Sens. 52 (3), 1761–1771. http://dx.doi.org/10.1109/TGRS.2013.2254494.

Peregrine, D.H., 1967. Long waves on a beach. J. Fluid Mech. 27 (4), 815–827.

Qi, Y., Wu, G., Liu, Y., Kim, M.-H., Yue, D.K.P., 2018a. Nonlinear phase-resolved reconstruction of irregular water waves. J. Fluid Mech. 838, 544–572. http://dx.doi.org/10.1017/jfm.2017.904.

Qi, Y., Wu, G., Liu, Y., Yue, D.K., 2018b. Predictable zone for phase-resolved reconstruction and forecast of irregular waves. Wave Motion 77, 195–213.

Raghukumar, K., Chang, G., Spada, F., Jones, C., Janssen, T., Gans, A., 2019. Performance characteristics of "spotter," a newly developed real-time wave measurement buoy. J. Atmos. Ocean. Technol. 36 (6), 1127–1141. http://dx.doi.org/10.1175/JTECH-D-18-0151.1.

Simanesew, A., Trulsen, K., Krogstad, H.E., Nieto Borge, J.C., 2017. Surface wave predictions in weakly nonlinear directional seas. Appl. Ocean Res. 65, 79–89. http://dx.doi.org/10.1016/j.apor.2017.03.009.

Thomson, J., 2012. Wave breaking dissipation observed with SWIFT drifters. J. Atmos. Ocean. Technol. 29 (12), 1866–1882. http://dx.doi.org/10.1175/JTECH-D-12-00018.1.

Thomson, J., Gemmrich, J., Rogers, W.E., Collins, C.O., Ardhuin, F., 2019. Wave groups observed in pancake sea ice. J. Geophys. Res.: Oceans 124 (11), 7400–7411. http://dx.doi.org/10.1029/2019JC015354.

Thomson, J., Girton, J.B., Jha, R., Trapani, A., 2018. Measurements of directional wave spectra and wind stress from a wave glider autonomous surface vehicle. J. Atmos. Ocean. Technol. 35 (2), 347–363. http://dx.doi.org/10.1175/JTECH-D-17-0091.1.

Thomson, J., Moulton, M., de Klerk, A., Talbert, J., Guerra, M., Kastner, S., Smith, M., Schwendeman, M., Zippel, S., Nylund, S., A new version of the SWIFT platform for waves, currents, and turbulence in the ocean surface layer, in: IEEE/OES Workshop on Currents, Waves, and Turbulence Measurements, 2019.

Toffoli, A., Gramstad, O., Trulsen, K., Monbaliu, J., Bitner-Gregersen, E., Onorato, M., 2010. Evolution of weakly nonlinear random directional waves: laboratory experiments and numerical simulations. J. Fluid Mech. 664, 313–336. http://dx.doi.org/10.1017/S002211201000385X.

WAFO-group, 2000. WAFO - A Matlab Toolbox for Analysis of Random Waves and Loads - A Tutorial. In: Math. Stat., Center for Math. Sci., Lund Univ., Lund, Sweden, URL: http://www.maths.lth.se/matstat/wafo.

Wu, G., 2004. Direct sImulation and Deterministic Prediction of Large-Scale Nonlinear Ocean Wave-Field (Ph.D. thesis). Massachusetts Institute of Technology. Dept. of Ocean Engineering.

Yoon, S., Kim, J., Choi, W., 2016. An explicit data assimilation scheme for a nonlinear wave prediction model based on a pseudo-spectral method. IEEE J. Ocean. Eng. 41 (1), 112–122. http://dx.doi.org/10.1109/JOE.2015.2406471.